nature communications

Article

https://doi.org/10.1038/s41467-026-68856-9

Acoustic shape-morphing micromachines

Received: 16 July 2025

Accepted: 19 January 2026

Published online: 02 February 2026

Check for updates

Xiaoyu Su[1,2,9], Lei Wang[2,9], Zhaozhong Wang[3], Le Yang[4], Mingjie Li[5], Dazhao Zhu[6], Zhijun Li[7], Weizheng Yuan[1], Honglong Chang[1] & Binglu Wang[8]

Shape-morphing mechanisms help organisms adapt to their environment and have inspired applications in advanced systems. Designing microrobots that are both miniaturized and capable of fast shape changes is challenging, as performance can be weakened at small scales. Ultrasound offers advantages such as fast response, repeatability, and programmability, making it suitable for enabling shape-morphing microrobots. Here, we introduce an acoustic micromachine composed of two microbubbles connected by a microhinge. Acoustic-field excitation generates interaction forces between the bubbles, enabling complete micromachine deformation within milliseconds. We also present design principles for programmable acoustic deformation, enabling both forward and inverse design, precise control, and information storage. By tuning the excitation amplitude, the micromachine can switch between multiple modes. As proof of concept, microlotus and microbird structures are demonstrated with controllable and stable performance.

Shape-morphing mechanism enables organisms to adapt to the environment, enhancing their chances of survival. For example, a pillbug defends itself against external threats by rolling its body into a tight sphere[1]. At the microscale, microorganisms achieve locomotion or predation through dynamic shape changes; for example, the spasmoneme in Vorticella can contract within milliseconds[2] (see Fig. 1a). Owing to their excellent environmental sensitivity and adaptability, these critical morphing mechanisms are widely applied to various macroscopic-scale systems, including robotic systems[3,4], wearable devices[5,6], medical devices[7–9], artificial muscles[6,10], and materials science[11,12]. However, most existing designs cannot maintain their superior shape-morphing characteristics while miniaturizing the structures. These designs often require tethered connections to external sources[13,14], significantly limiting their microscale applicability. Moreover, with increasing static friction and adhesion forces, surface forces, such as van der Waals and electrostatic forces, become predominant at the microscale. Consequently, small-scale structures typically maintain rigidity, showing high susceptibility toward fracture formation[15,16], thereby rendering the design of microscale variants highly challenging.

With rapid advancements in smart functional materials[17], micro/nano manufacturing technologies[18,19], precise manipulation[20–22], and multiphysics driving strategies[23–25], research on design frameworks and methodologies rooted in microscale shape-morphing mechanisms has seen substantial progress. These designs leverage characteristics, such as strong electrostatic adsorption, huge surface tension, and high area-mass ratio, endowing microrobots with advantages including high permeability, low immune rejection, and high local efficiency. As a result, they demonstrate significant potential across a range of fields, including biomedical engineering[26,27], microfluidics[28], and microactuation[29,30]. Besides, multiphysics field-driven methods are designed and used to control small untethered robots by using various stimuli, such as chemical gradients[31–34], light[35–39], heat[40–43], electric fields[30,44–47], and magnetic fields[48–51]. Although these designs address the challenges associated with microscale effects, substantial limitations exist. For example, pH-responsive hydrogel materials exhibit limited sensitivity and slow response because they can only react within a specific pH range. The choice of solvent can influence the behavior and applications of a material, thereby constraining its

[1]School of Mechanical Engineering, Northwestern Polytechnical University, Xi'an, China. [2]School of Advanced Manufacturing and Robotics, Peking University, Beijing, China. [3]School of Automation, Northwestern Polytechnical University, Xi'an, China. [4]School of Electronics and Control Engineering, Chang'an University, Xi'an, China. [5]Academy of Arts and Design, Tsinghua University, Beijing, China. [6]YZQ Instruments Co., Ltd., Hangzhou, China. [7]School of Mechanical Engineering, Tongji University, Shanghai, China. [8]School of Astronautics, Northwestern Polytechnical University, Xi'an, China. [9]These authors contributed equally: Xiaoyu Su, Lei Wang. e-mail: lei_wang@stu.pku.edu.cn; zjli@ieee.org; yuanwz@nwpu.edu.cn; changhl@nwpu.edu.cn; wbl921129@gmail.com

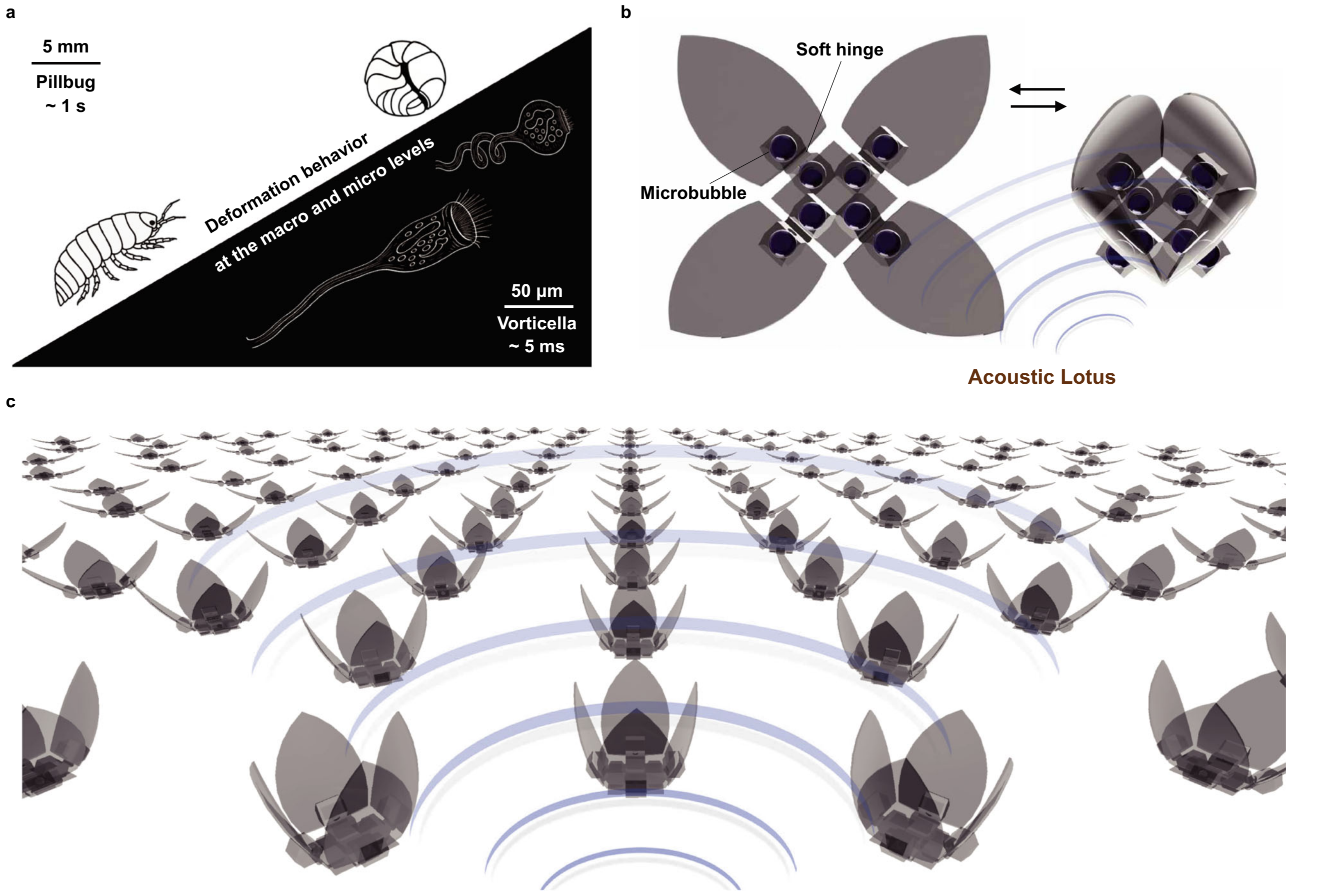

Fig. 1 | Morphing behavior of ASM. a Shape transformation occurs across different scales in nature, such as pillbug and vorticella. **b** Schematic of an untethered acoustic micromachine and its high-speed, reversible shape transformation in an acoustic field. **c** Schematic of a high-throughput ASM array.

potential utilization[52]. Consequently, the application of pH-responsive hydrogel deformation systems is limited for scenarios requiring rapid, repeatable, and frequency-programmable deformations. Shape memory alloys or polymers are commonly used as temperature-responsive deformable materials. However, their morphing mechanisms exhibit long response times and are difficult to miniaturize[53]. Furthermore, heating may be unsuitable or require stringent control in biological or temperature-sensitive environments. Photoresponsive morphing structures are constrained by environmental factors and photoresponsive materials are active within a limited wavelength range. Additionally, the scattering and reflection of light restrict the functionality and repeatability of photoresponsive morphing mechanisms[54]. Consequently, optically-actuated deformation systems are well-suited for environments with ample illumination, but are less applicable in scenarios that require actuation through opaque or highly scattering materials. Although deformation structures driven by electric and magnetic fields have attracted considerable attention[11,55], complex preprogramming, including predesigned magnetic moments, multilayer structures, and multistep processes, are required to produce micromachines compatible with such approaches. Furthermore, scaling down may lead to the failure or significant deterioration of the underlying physical mechanisms governing such designs.

Ultrasound fields exhibit several properties, such as high penetration, flexibility, low cost, and biocompatibility, and can generate significant power. Acoustic actuation methods based on sharp edges and microbubble-induced oscillations can generate intense local pressure gradients and fluid flows[56–59]. For instance, ultrasound-activated artificial ciliary bands mimic biological cilia to generate volumetric flow for cargo transport[57], while bubble-based microrobots demonstrate efficient propulsion through biological environments with the ability to adhere to soft tissues[58]. Despite exciting prospects, the use of acoustics in transformable micromachines has received minimal attention[60]. Controllable deformations at the microscale can be generated in micromachines using acoustics technology. These mechanisms can be miniaturized, remotely controlled, wirelessly operated, and rapidly fabricated for rapid and reversible switching within tens of milliseconds[60]. However, this deformation mechanism relies on differences in geometry and material stiffness, which makes it slow and power-hungry. Moreover, it struggles to reconfigure complex three-dimensional (3D) shapes or maintain stable deformation across different states. Therefore, research on the mechanisms, driving methods, and control techniques of acoustic micromachines is currently in the nascent stage, and a comprehensive theoretical framework for such systems has not been reported.

In this study, we designed an acoustic shape-morphing micromachines (ASMs) (see Fig. 1b) that can alter their shape within 10 ms under acoustic-field stimulation and rapidly return to their initial state on acoustic-field removal. These micromachines comprise a pair of identically sized microbubbles connected by flexible microhinges. On acoustic field exposure, microbubble oscillation induces deformation within milliseconds; the forces and torques required for this deformation are generated by secondary acoustic radiation forces between the microbubbles and the flow induced by their oscillations. This can be continuously tuned by varying the exciting acoustic-field voltage. Additionally, this study proposes a modular design approach for deformable micromachines based on their rapid response, ultrafast deformation, large deformation angles, and programmability properties. The motion of these machines can be predicted using Denavit-Hartenberg (DH) parameters, which can explain 2D-to-2D and 2D-to-

3D deformations. Subsequently, the potential of the proposed method for 3D-to-3D deformation is analyzed. The results offer different design paradigms for a wide range of applications at the microscale in various fields, including soft robotics, flexible electronics, microfluidics, smart materials, and adaptive optics.

Results

Design and Characterization of ASMs

Microbubbles are widely used as microscale acoustic tools. Compared with other tools, such as sharp-edged structures[61], microbubbles exhibit frequency response characteristics under external acoustic-field stimulation[62]. Additionally, interaction forces exist between different microbubbles[63]. These mechanisms offer greater flexibility in the design and characterization of microbubble-based micromachines, thereby enhancing their potential multifunctionality. Supplementary Figs. S1 and S3 show the working schematic and fabrication process of the ASM, respectively. Micromachines with hinges of varying lengths, ranging from 4 to 16 μm, width within the range of 0.5–3 μm, and a uniform height of 57.5 μm in the Z-direction were manufactured in this study. The deformable angle between the two microbubbles ranged from 0° to 75°. Supplementary Fig. S7 shows the rigid structure of the ASMs and Young's modulus of their flexible microhinges measured using an atomic force microscope (see Supplementary Note 1 and Supplementary Fig. S7 for details). Detailed information on the fabrication process is presented in the Materials and Methods section.

The characterization of the manufactured ASMs was experimentally investigated using a setup comprising an acoustic manipulation region and a piezoelectric transducer (PZT) adjacent to a glass slide (see Supplementary Fig. S2). The PZT was connected to a signal generator through an amplifier to produce an acoustic field with adjustable amplitude and frequency. The dynamic deformation of the ASMs was observed using a microscope and camera. An acoustic field with a voltage amplitude varying within the range of 0–60 V and a working frequency of 102-104 kHz, matching the resonance frequency of the experimental setup, was applied during the analysis. Further experimental details are provided in the Materials and Methods section.

A microbubble pair with identical diameters is a crucial component of ASMs as it determines the deformation capability of the entire device. When the acoustic field traverses the liquid medium and reaches the micromachine, acoustic streaming effects occur between the pair of microbubbles; secondary acoustic radiation forces induces attraction between the bubbles. Simultaneously, the microhinges contract, causing the two microbubbles to approach each other until complete contact, as shown in Fig. 2a, b. The ASMs manufactured in this study showed a fully folded shape within 5–10 ms, as indicated by the experimental results (see Supplementary movie S1). This dynamic deformation was controlled by the acoustic pressure; once the acoustic field was turned off, the ASMs rapidly returned to its original shape, as shown in Fig. 2c, d. Through structural design, the deformation in the XY-plane could be extended to the ZX-plane, as shown in Fig. 2e. After deformation of the ASMs, their microscopic images showed defocusing along the Z-axis, as illustrated in Fig. 2f, g. Notably, this dynamic deformation is regulated by the excitation voltage of the external acoustic field, which can be adjusted using a signal generator. The Materials and Methods section provides a detailed characterization of the acoustic pressure distribution generated by our setup, as well as the operational lifetime of the microbubbles in the ASM.

To further understand the mechanisms underlying shape morphing, the dynamic mechanisms of micromachines in an acoustic field were investigated. According to bubble acoustics, acoustically excited bubbles function as acoustic sources when they approach each other[63,64]. Because the distance between the bubbles is significantly smaller than the wavelength of the ultrasound in the experimental setup, the acoustic radiation force generated by the background acoustic field can be assumed to not cause relative displacement between the microbubbles. Therefore, the secondary forces acting on the micromachine comprised the interaction forces between the bubbles, resistance induced by acoustic streaming, and secondary acoustic radiation forces. As identical bubbles produce the same acoustic streaming, the interaction force between them is attractive, causing the adjacent microbubbles to move closer to each other. The total force acting on the microbubbles can be expressed as follows:

$$F_B = F_U + F_S + F_R \tag{1}$$

where F_U, F_S, and F_R represent the acoustic radiation force, thrust from the flow, and drag force exerted on a bubble by the flow generated by the neighboring bubbles, respectively. As the distance between the bubbles is comparable to the bubble size, which is significantly smaller than the wavelength of sound waves, in this study, we assumed that F_R did not depend on the distance between the microbubbles[65]. Therefore, we have $|F_R| = |F_S|$. Given that acoustic streaming is a second-order effect, its resulting thrust remains substantially smaller than the secondary acoustic radiation force at low-to-moderate drive levels with the microbubble approaching. According to the force balance equation[64,66], the above equation can be rewritten as

$$F_B \approx F_U = B^*G \tag{2}$$

$$G = \frac{r_1^2}{L^2}\frac{1}{[(1-\omega_0^2/\omega^2)^2+\delta_0^2]} \tag{3}$$

where $G > 0$ represents the attraction between the microbubbles. As shown in the Fig. 2a, r_1 represents the radius of the identical microbubble pairs, L denotes the distance between the microbubbles, ω_0 is the natural frequency of the microbubble pair, and ω is the acoustic excitation frequency. Moreover, δ_0 denotes their total damping constants. B is a scalar related to the excitation amplitude and does not change the sign of the force. Equation (3) indicates that the sign of the interaction force between the identical microbubbles remains constant, regardless of the changes in the acoustic excitation frequency. Therefore, the identical microbubbles tend to attract each other. However, the complex interaction forces between microbubbles of different sizes can result in attraction or repulsion depending on the acoustic excitation frequency. Details regarding to theoretical development, verification, and simulations of the model are provided in the Supplementary Information (see Supplementary Notes 2, 3 and Supplementary Fig. S4).

An intriguing phenomenon was observed on investigating the dynamics of the manufactured ASMs using high-magnification microscopy. As the two microbubbles were driven by a variable-amplitude acoustic field, the deformation amplitude of the micromachine changed with variations in the acoustic-field amplitude. The deformation amplitude of the micromachine remained constant at a constant acoustic-field amplitude. The introduction of tracer particles into the liquid generates microvortices in the surrounding fluid, as illustrated by the simulated streamlines in Supplementary Fig. S5, leading to rapid oscillation of the microbubbles. As the distance between the two microbubbles decreased, as per Equation (3), their interaction force increased significantly. Consequently, the microbubbles progressively attracted each other, inducing microhinge folding, resulting in a nonlinear reduction in the angle between the two microbubbles, as shown in Fig. 2h.

A series of experiments was conducted to optimize the microhinge structure of the ASMs for efficient transformation by varying their microhinge length, angle, and width. The deformation angle of the micromachine was significantly influenced by the microhinge width and length. At the microhinge length of 10 μm and an excitation

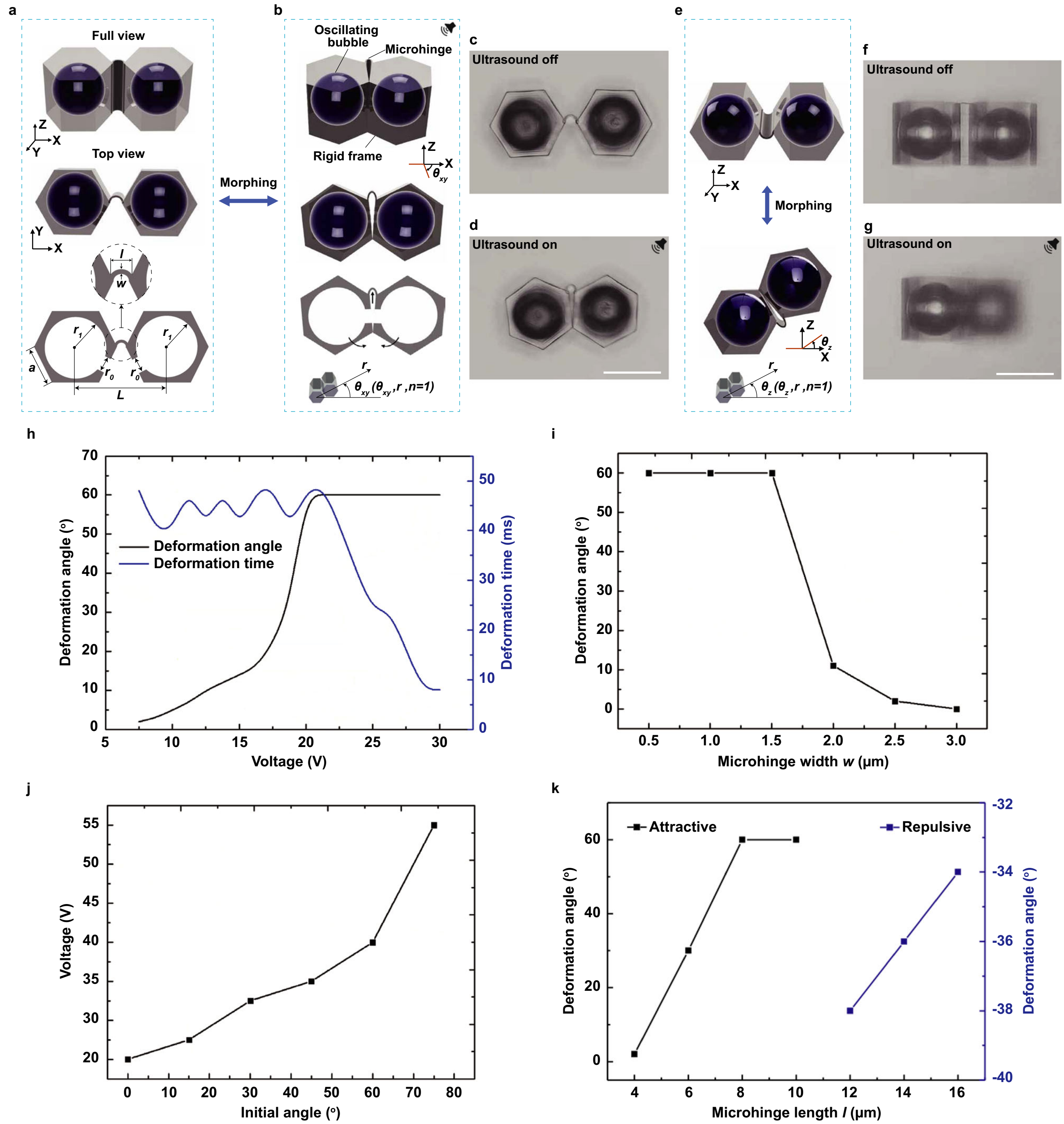

Fig. 2 | Characterization and optimization of the fabricated shape-morphing micromachine (ASM). a Schematic and design geometry of the ASM in the XY-plane. The basic structure of the ASM comprised a pair of microbubbles of the same diameter and a flexible microhinge connecting them. **b** Schematic of the ASM in the XY-plane after deformation under acoustic field excitation. The two microbubbles moved closer to each other, while the flexible microhinge showed bending. **c**,**d** Optical images of the initial and deformed ASM in the XY-plane. **e** Schematic and design geometry of an ASM in the ZX-plane. **f**,**g** Optical images of the initial and deformed ASM in the ZX-plane. **h** Effect of the acoustic field excitation voltage on the deformation angle and deformation time of the ASM with a microhinge length of 10 μm and a width of 1.5 μm. **i** Effect of microhinge width on the deformation angle of ASM with a microhinge length of 10 μm and a excitation voltage of 25 V. **j** Relationship between the initial angle of the ASM with a microhinge length of 10 μm and width of 1.5 μm and the excitation voltage required for its complete deformation. **k** Effect of microhinge length on the deformation angle of the ASM with a microhinge width of 1.5 μm and a excitation voltage of 60 V. Scale bars (for both images), 50 μm.

voltage of 25 V, a 25% reduction in the microhinge width (from 2 to 1.5 μm) resulted in a 445% increase (from 11° to 60°) in the maximum deformable angle, as shown in the Fig. 2i, possibly owing to a reduction in stiffness. Similarly, at the microhinge width of 1.5 μm, an increase of 33% in the microhinge length (from 6 to 8 μm) led to a substantial 100% increase (from 30° to 60°) in the maximum deformable angle. For microhinge lengths below 10 μm, the acoustic radiation force dominated the total force. The secondary acoustic radiation force reduces markedly with increased inter-microbubble distance. Under our experimental conditions, its attenuation upon microbubble separation $\frac{1}{L^2}$ thereby the streaming-induced thrust to become predominant. Consequently, when the microhinge length exceeded 10 μm, the magnitude of the acoustic radiation force decreased, and the thrust from the fluid became dominant, causing the sign of the total force to switch, resulting in the microbubbles beginning to repel each other, as shown in Fig. 2k.

Notably, the excitation voltage required for complete deformation increased with an increase in the initial ASM angle, as shown in Fig. 2j. The micromachine deformation time was investigated at different widths and excitation voltages. Upon only varying the external excitation voltage, the micromachine required 50–60 ms to deform completely. On full deformation, the deformation time decreased significantly with increasing excitation voltage; rapid deformation (8 ms) occurred at 60 V. Thin and long microhinges showed relatively low stiffness, and soft hinges generated greater acoustic forces, leading to more pronounced deformation. Moreover, by adjusting the laser intensity, the degree of microhinge cross-linking could be controlled by selectively enhancing the stiffness differential between the rigid link and soft hinge. These varied options for stiffness modulation provide exciting possibilities for designing and programming transformable micromachines and microrobots.

Design and Encoding of 2D ASMs

Unlike traditional 3D printing, shape-morphing micromachines should address complex forward and inverse design problems, making the model design crucial for precise experimentation. Considering the degrees of freedom and programmability of the ultrasonic deformation module, a modular design approach was used to analyze the forward and inverse kinematics of the target structure by defining the DH parameters associated with the deformation, which adhere to the principle of superposition. Any complex transformation can be described using only these four physical parameters in a closed-form analytical manner[67].

$$[T] = [XY_1][Z_1][XY_2][Z_2]\cdots[XY_n][Z_n] \tag{4}$$

Here, T denotes the transformation positioning the terminal link of the final building module. This transformation allows the frame structure to undergo curved motion around a defined axis.

$$[XY_i] = Trans_{xy_i}(R_{x_i})Trans_{y_i}(d_i)Rot_{xy_i}(\theta_{xy_i})Rot_{xy_i}(\alpha_{xy_i}) \tag{5}$$

$$[Z_i] = Trans_{z_i}(d_i)Rot_{z_i}(\theta_{z_i}) \tag{6}$$

where d_i, α_i, R_i, θ_i represent the DH parameters. In combination with the micromachine units described above, the DH parameters can be used to define the morphology planning principles of the modular system, as shown in Fig. 3a–i. Figure 3a–e shows the simulated rotational motion of micromachine units encoded using θ_i. These microunits were rigidly connected to each other to avoid inter-unit deformation interactions and ensure the validity of the superposition principle. The rotation angle of the microunits rotating around the Z-axis, determined by θ_{z_i}, can be adjusted by tuning the exposure dose during the manufacturing process. Figure 3f, g indicate that the radius of rotation, R_i, can be changed by connecting deformed microunits to the fixed microunits. Figure 3h shows the microunit offset along the Z-axis (d_i), which was used to construct the deformed morphology, and Fig. 3i shows that a coordinate system can be reconstructed by rotating the microcell in the XY-plane (α_i). Together, these four DH parameters can be used to formulate the morphological planning rules for the modularized system. The details regarding the theoretical development, validation, and simulations of the model are provided in the Supplementary Information (see Supplementary Fig. S11, Supplementary Tables S1, and S2, respectively).

According to the aforementioned rules, any 2D shape can be converted into a finite number of ASM modules. Here, the DH parameters were derived from inverse kinematics, and switching rules were constructed between the target and initial morphologies according to Equation (4), as shown in Fig. 4a. Figure 4d shows the details of the structure. Considering the deformation designs of the chain and wave to be the target and initial morphology, respectively, θ_i is the only variable parameter in the morphing design. Figure 4b, c show the experimental results of the chain-to-arc conversion (see Supplementary movie S2). Under the excitation voltage of 23 V, the chain structure folded sequentially, and the deformation of the four modules produced a deformation effect of up to 233°; complete folding and release occurred within 2003 and 742 ms, respectively, as shown in Fig. 4e. In the subsequent experiments, prior to the completion of folding, the response time increased with increasing voltage. When the excitation voltage exceeded the critical voltage of 23 V, at which full folding occurs, the time required for full folding gradually decreased with increasing voltage, finally requiring only 95 ms for a complete chain-to-arc deformation at the excitation voltage of 50 V. Additionally, Fig. 4f, i show transformations from chains to rolls, honeycombs, 'S's, and waves (see Supplementary movies S3–S6), confirming the versatility and generality of the proposed design approach.

Notably, multimodule micromachines that can store information can comprise modular unit assemblies (see Fig. 5). Multiple tailored configurations can be developed by encoding target traits according to the reverse-design method. Therefore, different information edits were implemented on the chain structure to enable the ASM to store the corresponding information. Here, the letters were encoded 'N', 'W', 'P', and 'U' (representing Northwestern Polytechnical University) in the chained 2D-ASM, as shown in Fig. 5a. The deformation process of each letter, which is the driving region of the deformed structure that gradually bends to the pre-edited position under the action of an externally stimulated acoustic field, was subsequently characterized, as shown in Fig. 5b–e and Supplementary movie S7. Thus, the ASM concept of information coding allows the creation of complex shape-coding systems with customized 2D transformations by tuning the design and layout of the deforming microunits.

Complex 3D-ASM

Blooming microlotus. To analyze the applicability of acoustic ASM technology, complex configurations of ASM in 3D space (labeled 3D-ASM) were investigated. In the aforementioned deformable micromodules, the interaction forces between bubbles under varying acoustic-field intensities enable them to maintain a stable state in any deformed configuration. Here, the deformation direction of the micromodules was adjusted to extend the deformation degrees of freedom along the Z-axis to design an acoustically driven microlotus inspired by the blooming of natural lotus flowers (see Fig. 6a). To address the constraints between structures, the flower comprised four petals connected to the center by ASM micromodules (see Fig. 6b). The driving force for structural deformation comprised interaction forces between a pair of identical acoustic-field-activated microbubbles. The deformation direction of the micromodules was configured to be along the Z-axis, resulting in a maximum deformation angle of 60° (see Supplementary movie S8). The deformation process was assessed in chronological order using one flower petal at a time. Unlike other deformation methods, such as those involving pH[52], thermal[53] and photonic stimuli[54], the deformation of the microlotus designed in this study could be halted at any moment and maintained in its current configuration by fixing the excitation voltage. On removing the ultrasonic excitation signal, the flowers rapidly returned to their initial state (see Supplementary Fig. S6). At the same time, the deformed microlotus could resist the external interference. On exposing the deformed microlotus to significant disturbances using a microprobe, the shape of the flower was restored within A few milliseconds (see Supplementary Note 5 and Supplementary Fig. S8). This deformation method,

https://doi.org/10.1038/s41467-026-68856-9

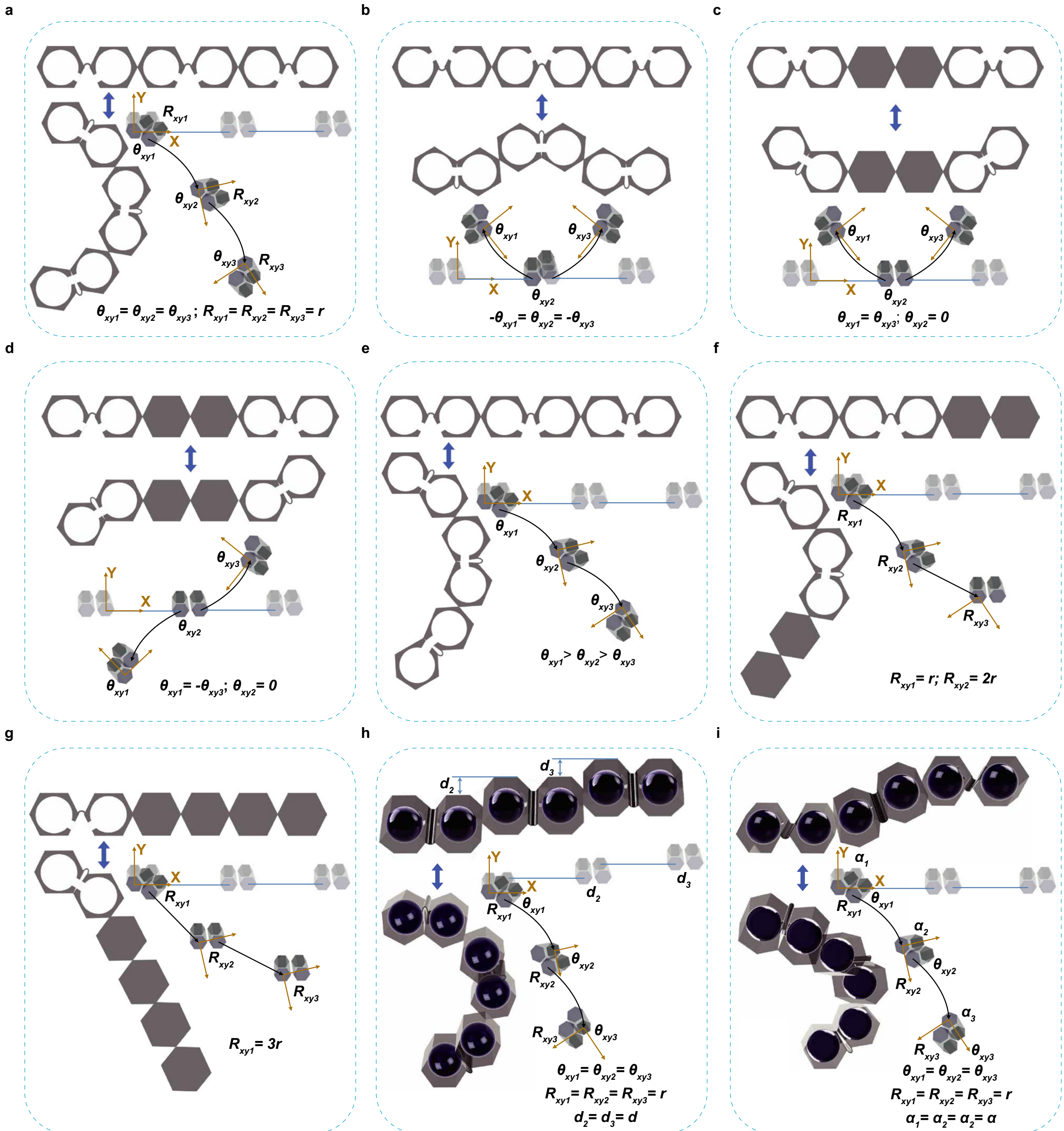

Fig. 3 | Design principles and rules for shape-morphing micromachine (ASM) modular systems. a–e Rotational deformation induced by the morphing of the ASM. Each ASM can be viewed as a combination of a rotational joint and a rigid bar, resembling a robotic arm. **f–i** Schematic of rotational movements with controlled amplitude and orientation enabled by the assembly of various preprogrammed ASMs. **a–i** Schematics showing the implementation of the four DH parameters d, α, R, and θ are implemented in our modular ASM.

which enabled the rapid opening and closing of the flower while maintaining its current state at any moment, could enable the precise 3D microscale-manipulation of microparticles, cells, or microrobots. We demonstrates a micromanipulation task where the magnetic cargo is delivered along a fixed track to a target location by the microlotus. The cargo is released upon the cessation of the acoustic excitation, as shown in Supplementary Fig. S15.

Figure 6c shows that the deformation time of the microlotus gradually decreased with increasing voltage. Under an external acoustic-field activation voltage of 30 V and frequency of 103 kHz, a maximum time of 621 ms was required for complete structural deformation (from the 'bloom' state to the 'bud' state). The resultant net force and net torque caused the micromachines to undergo transformation with a negative Poisson's ratio of approximately -1 (refer to Supplementary Note 4 and Supplementary Figs. S9 and S10 for calculation method and results). The time required for complete deformation decreased with increasing excitation voltage. At the acoustic-field activation voltage of 50 V, complete structural deformation occurred within 138 ms, resulting in a 77.8% reduction in response time as compared with that at the excitation voltage of 30 V. Figure 6e shows the optical images of the microlotus deformation process at the excitation voltage and frequency of 40 V and 103 kHz,

 https://doi.org/10.1038/s41467-026-68856-9

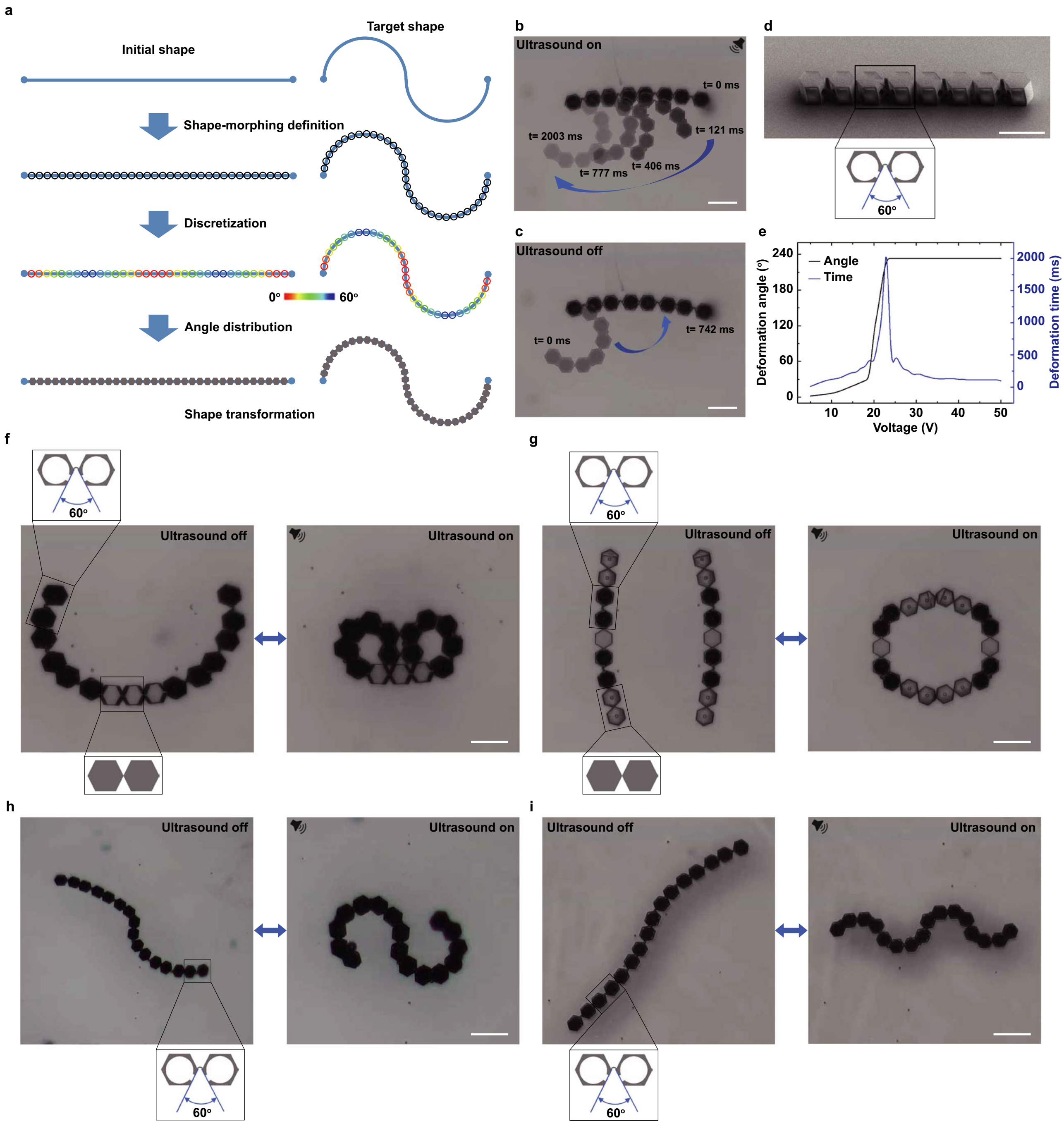

Fig. 4 | Inverse and forward design of morphing modular systems. a Inverse problem finding for programming a structure that morphs into the desired shape. For an arbitrary shape, such as a wave, the modular design converts it to a discrete counterpart with a finite number of joints and then obtains the DH parameters. The modular system subsequently constructs the shape transformation between the given wave shape and an assembled roll configuration by encoding the inversed θ_z into the roll, for it to morph into the shape of a wave. **b** The chain structure morph into an arc under sound field excitation, and the maximum time required for the ASM to complete the full deformation is 2003 ms. **c** After stopping the acoustic field excitation, the arc structure returned to the chain structure after 742 ms. **d** SEM images of the ASM. **e** Relationship between ASM deformation time and angle and sound field excitation voltage. **f**–**i** Optical images of the assembled morphing ASM encoded with different DH parameters. Scale bar (for both images), 100 μm.

respectively. Projection curves of the microlotus in the XY-plane at different deformation angles were used to correlate the optical images of the system with the degree of deformation (see Fig. 6d).

During the bubble's stable period, we cyclically actuated the microlotus at 103 kHz using sinusoidal voltages from 25 to 50 V. One cycle was defined as a full petal deformation and relaxation. By measuring cycle time and total bubble lifetime (see Supplementary Fig. S16), we estimated the maximal actuation cycles for each voltage. At 25 V, 545 cycles were possible before bubble shrinkage began. At 35 V, the actuation was faster, yielding 1403 cycles, though shrinkage accelerated slightly under stronger drive. At 50 V, despite larger deformation amplitude, the total lifetime dropped and the cycle count fell to 1136. These results reveal a trade-off: higher voltages yield faster and greater deformation but shorten microbubble longevity.

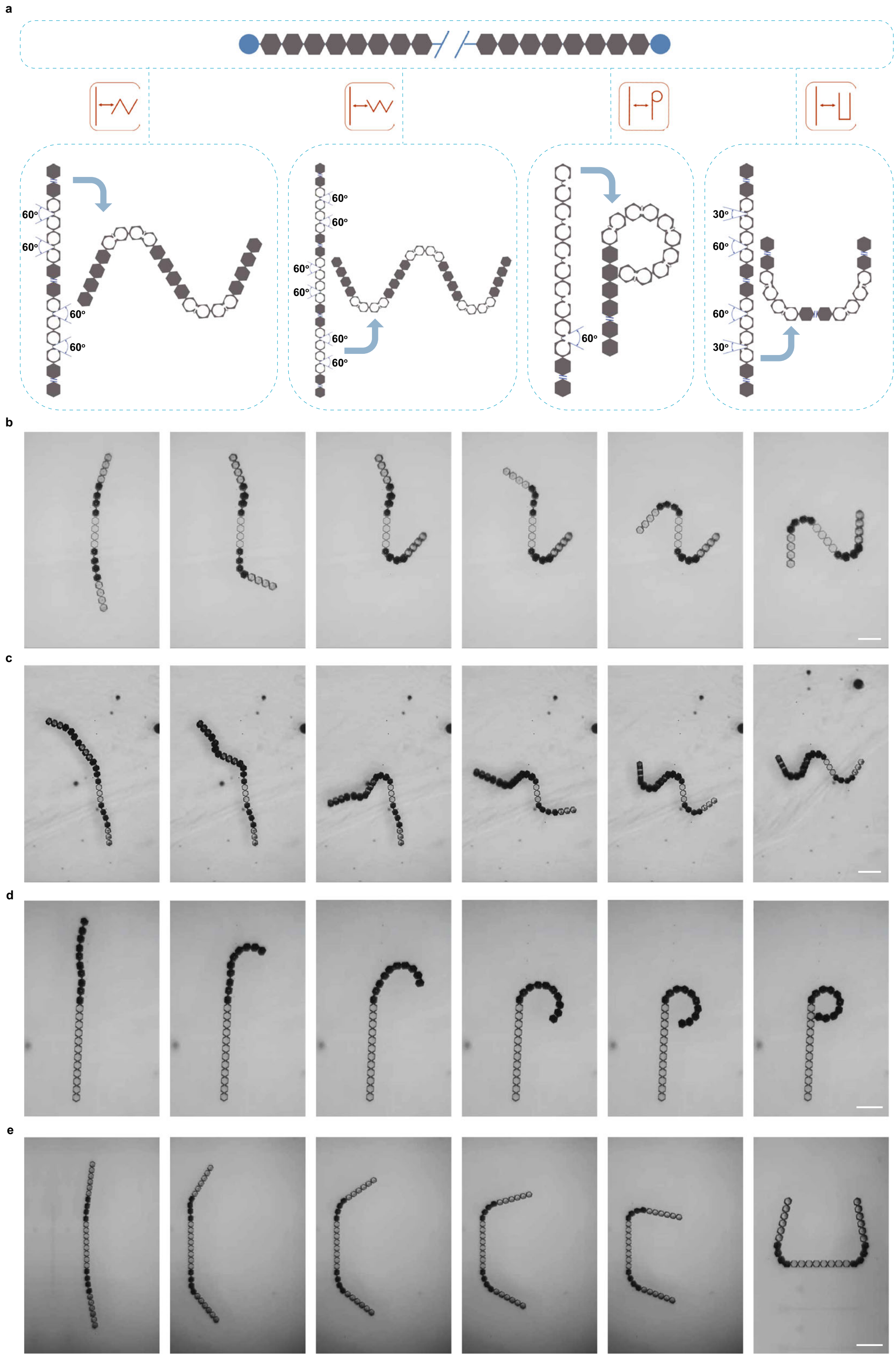

Fig. 5 | Encoding letters of the alphabet into ASM. a Conceptual design of ASM with a chain structure that can be encoded to transform into letters `N', `W', `P', and `U'. Each module in the schematic can be coded independently and the deformation angle can be selected independently. As a result, the characteristic positions of the chain structure will be deformed or fixed when acoustic field is applied. **b**–**e** Schematics and corresponding optical microscope images of the fabricated micromachines encoded for `N', `W', `P', and `U' shape morphing. The corresponding voltage of the excitation sound field is 30 V. Scale bar (for both the images), 200 μm.

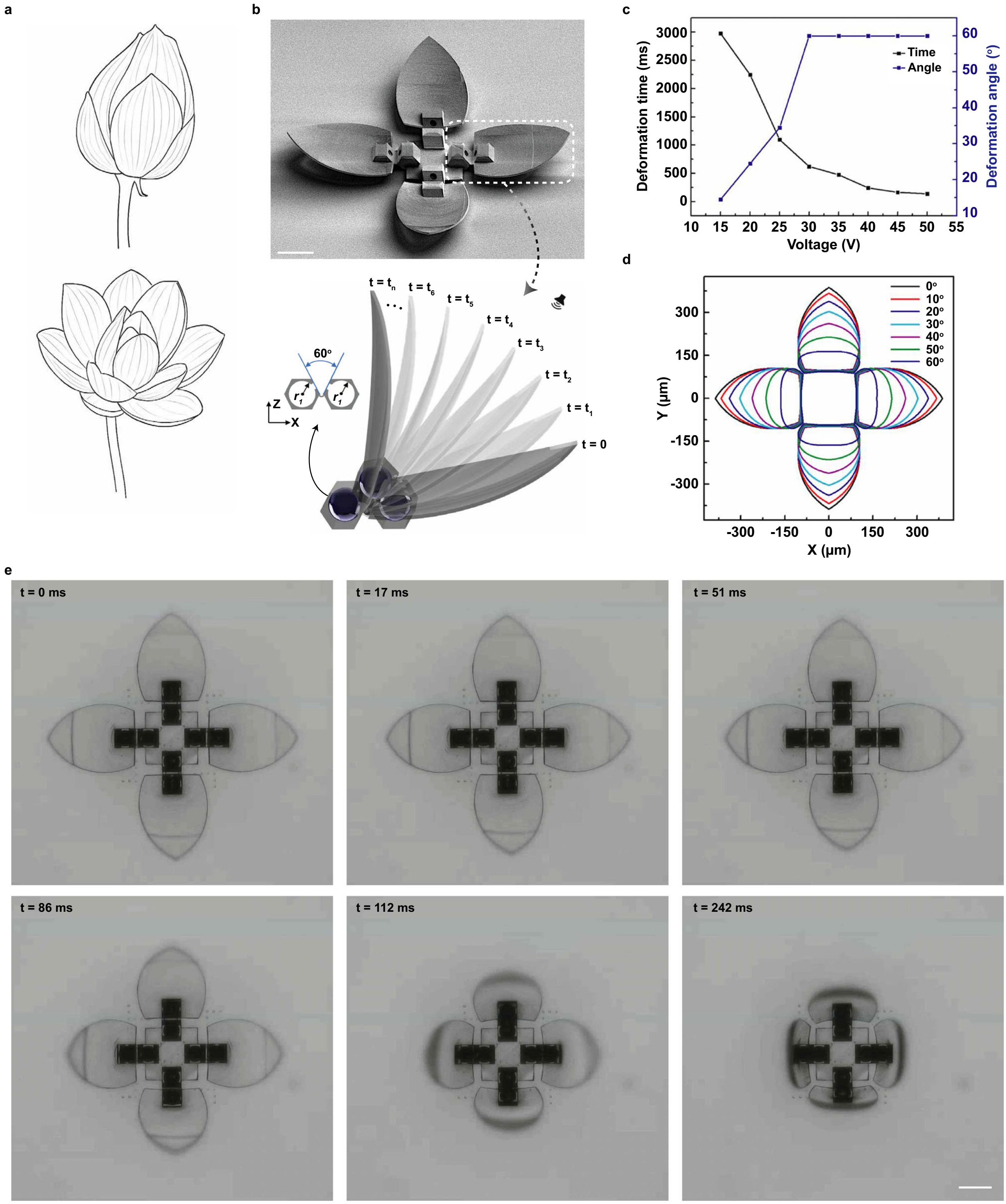

Fig. 6 | 3D microlotus with reversible transformation and infinite-mode. **a** Shape-morphing occurs in nature represented by a microlotus. **b** Schematic of an untethered acoustic micromachine and its high-speed, reversible shape transformation in an acoustic field. **c** Effect of the acoustic field excitation voltage on the microlotus deformation angle and time of the microlotus. **d** Projection curves for the microlotus on the XY-plane for different deformation angles. **e** Microlotus constructed from the `bloom state' folds into the `budding state' at the acoustic field excitation voltage of 40 V. Scale bar (for both the images), 100 μm.

Multiflight-mode microbird. Varying the deformation direction can result in advanced deformation behaviors, and the deformation amplitude can be tuned by adjusting the maximum deformation angle between the microbubbles within the ASM. Figure 7c shows two ASM units with different deformation directions oriented along the Z-axis while being distributed at different orientations in the XY-plane. Arbitrary deformation poses were assigned to each component by adjusting the deformation direction and amplitude of each ASM. As a

https://doi.org/10.1038/s41467-026-68856-9

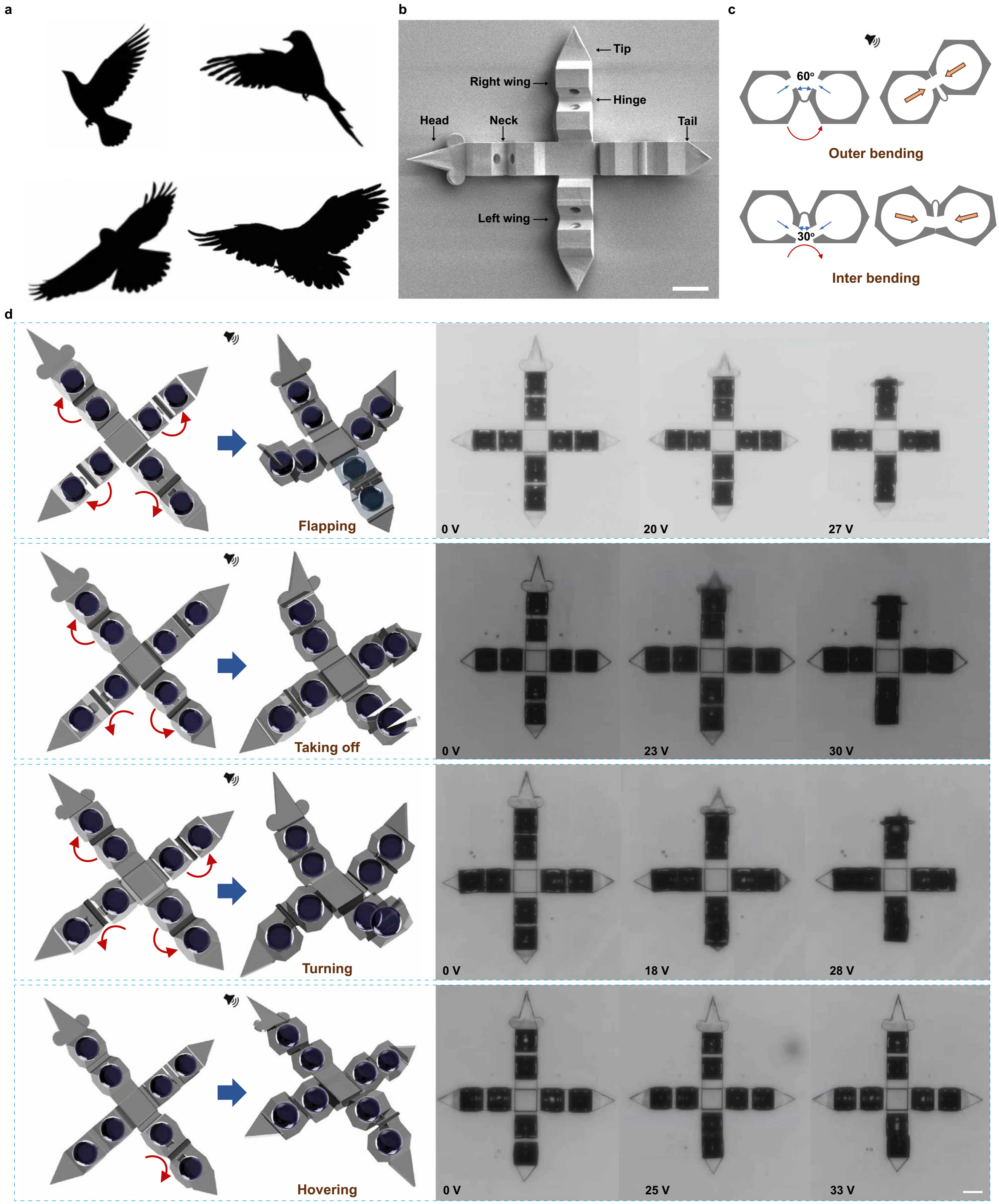

Fig. 7 | Origami-like microbird with multiple shape-morphing modes. a Multiple flying postures of birds in nature. **b** SEM image of the microbird. **c** Schematic of the morphing behaviors of the 3D ASM when actuated using an applied acoustic field. **d** Schematic (left) and optical images (right) of the microbird mimicking four flying modes: `flapping', `taking off', `turning', and `hovering'. From left to right in each row: schematic of a flat microbird with each direction of morphing in the 3D ASM; schematic showing the folding of the microbird under the acoustic field, and the optical microscope images of the experimental demonstrations. For each flying mode, the three optical images show the shape-morphing under an acoustic field with different intensities. Scale bar (for both the images), 50 μm.

proof-of-concept, an origami-type microbird was designed in this study to mimic the different flight modes of real birds (see Fig. 7a) by specifically arranging ASMs on the five body parts of the microbird (i.e., the head, body, tail, and a pair of wings). The corresponding electron microscopy image is shown in Fig. 7b. Two possible deformation directions and one stationary state existed at the wings or joints of the microbird. Editing the configurations of the ASMs on different parts of the microbird resulted in four distinct morphological changes, namely, 'flapping,' 'taking off,' 'turning,' and 'hovering' (see Fig. 7d and Supplementary movie S9). The microbird showed various deformation behaviors: in the 'flapping' mode, both the wings folded simultaneously in phase and in the same direction; in the 'taking off' mode, the head and tail rose, while the wings folded downward; in the 'turning' mode, the wings folded in different directions; and in the 'hovering' mode, only the tail folded relative to the body. Thus, the ASM can be used as a foundational structural module to design a wide range of microdeformable micromachines with diverse structural configurations, geometric dimensions, and deformation directions.

Discussion

Acoustically deformable micromachines, particularly those that utilize materials with varying stiffness, remain largely underexplored. This study reports an ASM based on the interaction forces between microbubbles connected by flexible microhinges that enable shape changes within milliseconds and rapidly return to their original state upon acoustic-field cessation. Simulations and theoretical analyses were used to validate this shape-transformation mechanism. Additionally, to address the forward and inverse problems of complex deformable structures and explore information storage, a 2D programmable design method for ASM-based micromodules is proposed in this study. The proposed device shows excellent reliability, stability, and flexibility in complex 3D-to-3D shape-morphing micromachines, such as blooming microlotus and microbirds with multiple flight modes, which are capable of withstanding external disturbances under various amplitudes of acoustic-field excitation and can be designed for specific purposes.

In microfluidics, integrating micromachines into microchip platforms can facilitate their application in drug delivery, object loading, and controlled screening. In metamaterials, complex arrays of deformable microstructures can be designed for optical steering, acoustic guidance, and energy amplification. In microrobotics, acoustically deformable micromachines can provide a design paradigm for acoustic microrobots, enhancing their maneuverability and environmental adaptability through functionalities, such as precise motion and navigation. In flexible electronic devices, deformable micromachines can facilitate enhanced interactions, information transmission, and functional development. Furthermore, in the near future, owing to the high compatibility of acoustic fields with biological tissues, these micromachines may be applied in blood vessels and the gastrointestinal tract in biomedicine.

Our study indicates that controllable ASMs hold great potential for application across multiple fields. However, they still face certain limitations, such as inaccuracy of output force and difficulty of programmable self-assembly. While our current design enables micromachines to switch between different shapes and modes, we aim to combine ultrasound and magnetic fields in the future to facilitate the motion and navigation of micromachines. Furthermore, we will focus on the automation and control aspects of ASMs, with plans to develop an ASM incorporating a mixture of microbubbles of different sizes. As microbubbles of varying sizes have distinct resonant frequencies, they can selectively activate the micromachines. In the future, we will also investigate the interactions of multiple ASMs under ultrasound stimulation.

Methods

Preparations of Materials

Acrylic ester (AAm, 99%), N-isopropylacrylamide (NIPAAm, 98%), ethyl lactate (EL, 98%), polyvinylpyrrolidone (PVP, average molecular weight, 1,300,000), N,N-dimethylformamide (DMF, 99.5%), 4,4′-bis(-diethylamino)benzophenone (EMK, 97%), Dipentaerythritol pentaacrylate (DPEPA, 98%), and triethanolamine (TEA, 99%) were purchased from Aladdin Chemicals. All chemicals were used directly as received.

Preparation of hydrogel precursor

In a typical procedure, NIPAAm and AAm were added to EL solution and stirred vigorously for 30 min. PVP was added to adjust the photoresist viscosity to Adjust the density of the cross-linked network in the material after polymerization. After complete dissolution, the above solution, DPEPA cross-linker, TEA photosensitizer, and the EMK/DMF photoinitiator solution were mixed and stirred overnight to ensure the complete mixing of each component in the solution. Once made, the photoresist was stored in yellow light condition to prevent unnecessary exposure before use.

In this study, NIPAAm served as a copolymeric component within the hydrogel network rather than as a thermoresponsive actuator. All experiments were conducted at room temperature (22 °C ± 3°C), well below the hydrogel's lower critical solution temperature (LCST) (~32 °C). Moreover, copolymerization with non-thermosensitive monomers (e.g., AAm) further elevates the LCST, ensuring no phase transition or change in hydrophilicity. Consequently, the material exhibits stable mechanical properties without temperature-induced deformation.

Fabrication of micromachine

Micromachine were fabricated by two-step sequential printing, using a commercial two-photon direct laser writing system (MPD-PPI, YZQ instruments). 3D models were built using the AutoCAD software and exported as STL format files. The STL files were converted into General Writing Language by the slicing software and loaded into the fabrication software for printing.

Before the first printing, the borosilicate glass square substrate (22 × 22 mm, 0.13 to 0.17 mm thick; Thermo Fisher Scientific Inc.) was rinsed using isopropanol, followed by nitrogen purging and oxygen plasma treatment, to serve as the printing substrate. To make certain printed microstructure pinned to the borosilicate glass, the substrate must be cleaned and locally surface-treated so the printed polymer forms a strong attachment.

Subsequently, a drop of IP-L resist was placed on the center of the substrate using a pipette, which was printed with a commercially available 3D laser lithography system (MPD-PPI, YZQ instruments) with a 60x/1.42 oil immersion objective (Olympus). During the first printing, the laser power (40 mW) and scanning speed ("8000 μ*m*/s") were set to cross-link the IP-L resist. After the first printing, the sample was immersed separately in SU-8 developer and IPA for 8 min and 5 min, respectively, for development, and then dried under nitrogen.

The IP-L resist was dropped on the existing structure on the glass substrate, which was placed back in the DLW system in the same position as the first printing. Before the second printing, the center of the printing stage was adjusted with the fabrication software through the integrated camera in the printing system to align with the existing structure. During the second printing, the laser power (40 mW) and scanning speed ("4000 μ*m*/s") were set to cross-link the hydrogel. The laser power and scanning speed were modulated dynamically to achieve desired stiffness and hardness. After the second printing, the sample was developed in IPA two times for 8 minutes and then dried under nitrogen. After the second fabrication, the flexible part and the rigid part are connected together.

Acoustic device

The acoustic system is established on a glass slide of 75 mm*25 mm*1 mm, where the transducer (Murata) is connected to the epoxy resin (Devocon). Once the microchannels and other microstructures are fabricated and cleaned on the acoustic device (IPA, Aladdin), they are transferred to the microscope stage. Upon immersion of the device into deionized water, small air pockets were naturally trapped within the microcavities due to incomplete wetting of the hydrophobic cavity surfaces. The cavity geometry (diameter = 50 *μm*) and high contact angle prevented full liquid infiltration, resulting in air entrapment. The trapped air was stabilized by surface tension pinning at the cavity rim, leading to the formation of persistent microbubbles within the device. Localized stiction of the movable structures was then overcome using a micromanipulator equipped with a metallic probe, which carefully released them without disturbing adjacent features. Then, the piezoelectric transducer is connected to the signal generator through an amplifier (ATA-2032 High Voltage Amplifier, Aigtek), with the purpose of generating a tunable frequency sound field in the liquid. The entire device is mounted under a microscope (CM4000, HangZhou BoNa Optoelectronics Co., Ltd.).

The transducer and acoustic chamber were securely mounted on a glass slide, with their position and orientation relative to the work area remaining unchanged throughout the experimental process. The design and calibration of the integrated acoustic chamber-transducer assembly were aimed at ensuring a reproducible and Uniform acoustic field. Furthermore, the experimental setup remained unaltered between trials, thereby maintaining a spatially homogeneous acoustic field. The specific positional relationship is illustrated in the Supplementary Fig. S14a. Acoustic field simulations under this configuration were also performed, as shown in the Supplementary Fig. S14b. It can be observed that when the printed structure is positioned at the center of the acoustic chamber—a condition readily achievable in two-photon direct laser writing fabrication—it is subjected to a uniform acoustic field under 103 kHz ultrasound excitation.

We characterized the microbubble lifetime in deionized water and PBS buffer, as shown in Supplementary Fig. S13. It was observed that in the absence of ultrasonic excitation, the microbubble maintained its volume without change for 25 min in deionized water. Under ultrasonic excitation at 25 V (exceeding the minimum actuation voltage for complete deformation of the ASM), the operational duration of the microbubble decreased to 8 min, as shown in Fig. S13a. Using PBS buffer as the liquid medium can increase the lifetime of the microbubble. Without ultrasonic excitation, the microbubble maintained a constant volume for 64 min, representing a 156% increase compared to its lifetime in deionized water. Under 25 V ultrasonic excitation, the working time reached 29 min, a 263% increase over that in deionized water, as presented in Fig. S13b. Thus, through experimental configuration, sufficient operational time for the ASM can be secured, during which the microbubble volume remains constant. Under our experimental conditions, this ensures that the ASMs maintain in-phase vibrations and ultimately undergo mutual attraction under ultrasonic excitation.

Imaging and data analysis

Experiments were conducted on a microscope (CM4000, HangZhou BoNa Optoelectronics Co., Ltd.). The microscope was equipped with a camera and the recorded frequencies were analyzed using software. Recording frame rates range from 50 to1000 frames per second (fps). Recorded footage is analyzed in ImageJ.

Numerical Simulation

The interaction forces between microbubbles were analyzed and calculated using commercial software MATLAB. The numerical simulation reported in this work was performed using the commercial multiphysics finite element software COMSOL. Two-dimensional simulations were conducted using triangular elements, while three-dimensional simulations were conducted using tetrahedral elements to simplify the meshing process. We assumed the acoustic field to be a linearized first-order field of the Navier-Stokes equations, and the acoustic flow field to be a time-averaged second-order field describing system disturbances. We used $P_1 - P_2$ composite elements to measure pressure and velocity, where P_1 and P_2 represent triangular elements with 1st and 2nd order Lagrange polynomials, respectively. Direct solvers were employed for both first and second-order equation systems to obtain solutions.

Data availability

The authors declare that the main data supporting the findings of this study are available within the article and its Supplementary Information. Extra data are available from the corresponding authors upon request. Source data are provided with this paper.

References

1. Paul, N. et al. Ligand-directed shape reconfiguration in inorganic materials. *Small* **20**, 2305460 (2024).
2. Böttger, T., van Oorschot, B. K., Pepper, R. E. The effect of external flow on 3D orientation of a microscopic sessile suspension feeder, Vorticella convallaria. *Ann. New York Acad. Sci.* **1537**, 51–63 (2024).
3. Sun, J., Lerner, E., Tighe, B., Middlemist, C. & Zhao, J. Embedded shape morphing for morphologically adaptive robots. *Nat. Commun.* **14**, 6023 (2023).
4. Kotikian, A. et al. Untethered soft robotic matter with passive control of shape morphing and propulsion. *Sci. Robot.* **4**, eaax7044 (2019).
5. Qin, F. et al. ExoForm: Shape memory and self-fusing semi-rigid wearables, in *Extended Abstracts of the 2021 CHI Conference on Human Factors in Computing Systems* pp. 1–8 (CHI, 2021).
6. Fei, F. et al. Cephalopod-inspired stretchable self-morphing skin via embedded printing and twisted spiral artificial muscles. *Adv. Funct. Mater.* **31**, 2105528 (2021).
7. Zarek, M., Mansour, N., Shapira, S. & Cohn, D. 4D printing of shape memory-based personalized endoluminal medical devices. *Macromol. Rapid Commun.* **38**, 1600628 (2017).
8. Qu, G. et al. Smart implants: 4D-printed shape-morphing scaffolds for medical implantation. *Int. J. Bioprint.* **9**, 764 (2023).
9. Mohagheghian, E. et al. Quantifying stiffness and forces of tumor colonies and embryos using a magnetic microrobot. *Sci. Robot.* **8**, eadc9800 (2023).
10. Yang, Z. et al. Precisely controllable artificial muscle with continuous morphing based on "breathing" of supramolecular columns. *Adv. Mater.* **35**, 2211648 (2023).
11. Bastola, A. K. & Hossain, M. The shape–morphing performance of magnetoactive soft materials. *Mater. Des.* **211**, 110172 (2021).
12. Oliver, K., Seddon, A. & Trask, R. S. Morphing in nature and beyond: a review of natural and synthetic shape-changing materials and mechanisms. *J. Mater. Sci.* **51**, 10663–10689 (2016).
13. Ma, K. Y., Chirarattananon, P., Fuller, S. B. & Wood, R. J. Controlled flight of a biologically inspired, insect-scale robot. *Science* **340**, 603–607 (2013).
14. Ma, K. Y., Felton, S. M., Wood, R. J. Design, fabrication, and modeling of the split actuator microrobotic bee, in *2012 IEEE/RSJ International Conference on Intelligent Robots and Systems* pp. 1133–1140 (IEEE, 2012).
15. Purcell, E. M. Life at low Reynolds number, in *Physics and our world: reissue of the proceedings of a symposium in honor of Victor F Weisskopf*, 47–67 (World Scientific, 2014).
16. Bazant, Z. P. *Scaling of structural strength* (Elsevier, 2005).
17. Zeng, H. et al. High-resolution 3D direct laser writing for liquid-crystalline elastomer microstructures. *Adv. Mater.* **26**, 2319–2322 (2014).
18. Schaedler, T. A. et al. Ultralight metallic microlattices. *Science* **334**, 962–965 (2011).
19. Heuthe, V.-L., Panizon, E., Gu, H. & Bechinger, C. Counterfactual rewards promote collective transport using individually controlled swarm microrobots. *Sci. Robot.* **9**, eado5888 (2024).
20. Alogla, A. et al. Micro-tweezers: design, fabrication, simulation and testing of a pneumatically actuated micro-gripper for micromanipulation and microtactile sensing. *Sens. Actuators A Phys.* **236**, 394–404 (2015).
21. Power, M., Thompson, A. J., Anastasova, S. & Yang, G.-Z. A monolithic force-sensitive 3D microgripper fabricated on the tip of an

optical fiber using 2-photon polymerization. *Small* **14**, 1703964 (2018).
22. Han, H. et al. Imaging-guided bioresorbable acoustic hydrogel microrobots. *Sci. Robot.* **9**, eadp3593 (2024).
23. Xia, H. et al. Ferrofluids for fabrication of remotely controllable micro-nanomachines by two-photon polymerization. *Adv. Mater.* **22**, 3204–3207 (2010).
24. Chen, X.-Z. et al. Hybrid magnetoelectric nanowires for nanorobotic applications: fabrication, magnetoelectric coupling, and magnetically assisted in vitro targeted drug delivery. *Adv. Mater.* **29**, 1605458 (2017).
25. Li, N. et al. Human-scale navigation of magnetic microrobots in hepatic arteries. *Sci. Robot.* **9**, eadh8702 (2024).
26. Kuo, J.-C., Huang, H.-W., Tung, S.-W. & Yang, Y.-J. A hydrogel-based intravascular microgripper manipulated using magnetic fields. *Sens. Actuators A Phys.* **211**, 121–130 (2014).
27. Yang, L. et al. Targeted single-cell therapeutics with magnetic tubular micromotor by one-step exposure of structured femtosecond optical vortices. *Adv. Funct. Mater.* **29**, 1905745 (2019).
28. Jamal, M., Zarafshar, A. M. & Gracias, D. H. Differentially photo-crosslinked polymers enable self-assembling microfluidics. *Nat. Commun.* **2**, 527 (2011).
29. Kim, H. et al. Shape morphing smart 3D actuator materials for micro soft robot. *Mater. Today* **41**, 243–269 (2020).
30. Liu, Q. et al. Micrometer-sized electrically programmable shape-memory actuators for low-power microrobotics. *Sci. Robot.* **6**, eabe6663 (2021).
31. Hu, Y. et al. Botanical-inspired 4D printing of hydrogel at the microscale. *Adv. Funct. Mater.* **30**, 1907377 (2020).
32. Huang, T.-Y. et al. Four-dimensional micro-building blocks. *Sci. Adv.* **6**, eaav8219 (2020).
33. Narupai, B., Smith, P. T. & Nelson, A. 4D printing of multi-stimuli responsive protein-based hydrogels for autonomous shape transformations. *Adv. Funct. Mater.* **31**, 2011012 (2021).
34. Dong, Y. et al. 4D printed hydrogels: fabrication, materials, and applications. *Adv. Mater. Technol.* **5**, 2000034 (2020).
35. Cheng, Y.-C., Lu, H.-C., Lee, X., Zeng, H. & Priimagi, A. Kirigami-based light-induced shape-morphing and locomotion. *Adv. Mater.* **32**, 1906233 (2020).
36. Lv, J.-A. et al. Photocontrol of fluid slugs in liquid crystal polymer microactuators. *Nature* **537**, 179–184 (2016).
37. Chen, Y. et al. Light-driven dandelion-inspired microfliers. *Nat. Commun.* **14**, 3036 (2023).
38. Wang, Y. et al. Light-activated shape morphing and light-tracking materials using biopolymer-based programmable photonic nanostructures. *Nat. Commun.* **12**, 1651 (2021).
39. Zhang, Z. & Ahmed, D. Light-driven high-precision cell adhesion kinetics. *Light. Sci. Appl.* **11**, 266 (2022).
40. Hwang, D., Barron III, E. J., Haque, A. T. & Bartlett, M. D. Shape morphing mechanical metamaterials through reversible plasticity. *Sci. Robot.* **7**, eabg2171 (2022).
41. Aharoni, H., Xia, Y., Zhang, X., Kamien, R. D. & Yang, S. Universal inverse design of surfaces with thin nematic elastomer sheets. *Proc. Natl. Acad. Sci. USA* **115**, 7206–7211 (2018).
42. Ding, Z. et al. Direct 4D printing via active composite materials. *Sci. Adv.* **3**, e1602890 (2017).
43. Zheng, Z. et al. Electrodeposited superhydrophilic-superhydrophobic composites for untethered multi-stimuli-responsive soft millirobots. *Adv. Sci.* **10**, 2302409 (2023).
44. He, Q. et al. Electrically controlled liquid crystal elastomer–based soft tubular actuator with multimodal actuation. *Sci. Adv.* **5**, eaax5746 (2019).
45. Wang, W. et al. Cilia metasurfaces for electronically programmable microfluidic manipulation. *Nature* **605**, 681–686 (2022).
46. Miskin, M. Z. et al. Electronically integrated, mass-manufactured, microscopic robots. *Nature* **584**, 557–561 (2020).
47. Reynolds, M. F. et al. Microscopic robots with onboard digital control. *Sci. Robot.* **7**, eabq2296 (2022).
48. Hu, X. et al. Magnetic soft micromachines made of linked micro-actuator networks. *Sci. Adv.* **7**, eabe8436 (2021).
49. Zhang, S. et al. 3D-printed micrometer-scale wireless magnetic cilia with metachronal programmability. *Sci. Adv.* **9**, eadf9462 (2023).
50. Alapan, Y., Karacakol, A. C., Guzelhan, S. N., Isik, I. & Sitti, M. Reprogrammable shape morphing of magnetic soft machines. *Sci. Adv.* **6**, eabc6414 (2020).
51. Ji, S., Li, X., Chen, Q., Lv, P. & Duan, H. Enhanced locomotion of shape morphing microrobots by surface coating. *Adv. Intell. Syst.* **3**, 2000270 (2021).
52. Chen, Q., Lv, P., Huang, J., Huang, T.-Y., Duan, H. Intelligent shape-morphing micromachines. *Research* **2021**, 9806463 (2021).
53. Kim, M.-S. et al. Shape memory alloy (SMA) actuators: the role of material, form, and scaling effects. *Adv. Mater.* **35**, 2208517 (2023).
54. Yang, M. et al. Photoresponsive actuators built from carbon-based soft materials. *Adv. Opt. Mater.* **7**, 1900069 (2019).
55. Ahn, J. et al. A review of recent advances in electrically driven polymer-based flexible actuators: smart materials, structures, and their applications. *Adv. Mater. Technol.* **7**, 2200041 (2022).
56. Deng, Y., Paskert, A., Zhang, Z., Wittkowski, R. & Ahmed, D. An acoustically controlled helical microrobot. *Sci. Adv.* **9**, eadh5260 (2023).
57. Dillinger, C., Nama, N. & Ahmed, D. Ultrasound-activated ciliary bands for microrobotic systems inspired by starfish. *Nat. Commun.* **12**, 6455 (2021).
58. Lee, J. G. et al. Bubble-based microrobots with rapid circular motions for epithelial pinning and drug delivery. *Small* **19**, 2300409 (2023).
59. Xiao, Y., Zhang, J., Fang, B., Zhao, X. & Hao, N. Acoustics-actuated microrobots. *Micromachines* **13**, 481 (2022).
60. Zhang, Z., Shi, Z. & Ahmed, D. SonoTransformers: transformable acoustically activated wireless microscale machines. *Proc. Natl. Acad. Sci. USA* **121**, e2314661121 (2024).
61. Harley, W. S., Kolesnik, K., Heath, D. E. & Collins, D. J. Enhanced acoustic streaming effects via sharp-edged 3D microstructures. *Lab a Chip* **24**, 1626–1635 (2024).
62. Wei, Y., Lu, X., Bao, J., Zhang, S. & Wu, D. Acoustic-based micro-bubble grippers for automatic on-chip selection of spherical microrobot models. *Adv. Mater. Technol.* **9**, 2301455 (2024).
63. Kaynak, M., Dolev, A. & Sakar, M. S. 3D printed acoustically programmable soft microactuators. *Soft Robot.* **10**, 246–257 (2023).
64. Doinikov, A. & Zavtrak, S. On the mutual interaction of two gas bubbles in a sound field. *Phys. Fluids* **7**, 1923–1930 (1995).
65. Bruus, H. Acoustofluidics 10: scaling laws in acoustophoresis. *Lab a Chip* **12**, 1578–1586 (2012).
66. Doinikov, A. A. Bjerknes forces and translational bubble dynamics. *Bubble Part. Dyn. Acoust. Fields Mod. Trends Appl.* **661**, 95–143 (2005).
67. Denavit, J., Hartenberg, R. S. A kinematic notation for lower-pair mechanisms based on matrices. *J. Appl. Mech.* **22**, 215–221 (1955).

Acknowledgements

We acknowledge financial support from the Key Projects in Shaanxi Province (No.2024CY2-GJHX-08), the Key Projects in Shaanxi Province (No.2024CY2-GJHX-10) and China Postdoctoral Science Foundation (No.2023M740091)

Author contributions

X.S. and L.W. contributed equally as co-first authors and are listed in alphabetical order. Both co-first authors agree that either author may list themselves first on a CV. Correspondence to L.W., W.Y., H.C. or B.W.

X.S., L.W., B.W., W.Y., H.C., and Z.L. conceived the project. D.Z. and X.S. developed the fabrication process. X.S. developed the design strategy of acoustic shape-mophing micromachines. X.S. tested the shape-morphing performance. X.S., L.W., Z.W., L.Y., M.L., and B.W. worked on the manuscript together. All authors contributed to the discussion of the results and the manuscript revision. L.W. and X.S. contributed to the revision of the manuscript, including responding to reviewer comments and refining the data analysis.

Competing interests

The authors declare no competing interests.

Additional information

Supplementary information The online version contains supplementary material available at https://doi.org/10.1038/s41467-026-68856-9.

Correspondence and requests for materials should be addressed to Lei Wang, Zhijun Li, Weizheng Yuan, Honglong Chang or Binglu Wang.

Peer review information *Nature Communications* thanks Sang Kug Chung, David Collins and Joseph Rich for their contribution to the peer review of this work. A peer review file is available.